

# Extended depth-range profilometry using the phase-difference and phase-sum of two close-sensitivity projected fringes

MANUEL SERVIN,\* MOISES PADILLA, AND GUILLERMO GARNICA

<sup>1</sup>Centro de Investigaciones en Optica A. C., 37000 Leon Guanajuato, Mexico.

\*[mservin@cio.mx](mailto:mservin@cio.mx)

**Abstract:** We propose a high signal-to-noise extended depth-range three-dimensional (3D) profilometer projecting two linear-fringes with close phase-sensitivity. We use temporal phase-shifting algorithms (PSAs) to phase-demodulate the two close sensitivity phases. Then we calculate their phase-difference and their phase-sum. If the sensitivity between the two phases is close enough, their phase-difference is not-wrapped. The non-wrapped phase-difference as extended-range profilometry is well known and has been widely used. However as this paper shows, the closeness between the two demodulated phases makes their difference quite noisy. On the other hand, as we show, their phase-sum has a much higher phase-sensitivity and signal-to-noise ratio but it is highly wrapped. Spatial unwrapping of the phase-sum is precluded for separate or highly discontinuous objects. However it is possible to unwrap the phase-sum by using the phase-difference as first approximation and our previously published 2-step temporal phase-unwrapping. Therefore the proposed profilometry technique allows unwrapping the higher sensitivity phase-sum using the noisier phase-difference as stepping stone. Due to the non-linear nature of the extended 2-steps temporal-unwrapper, the harmonics and noise errors in the phase-difference do not propagate towards the unwrapping phase-sum. To the best of our knowledge this is the highest signal-to-noise ratio, extended depth-range, 3D digital profilometry technique reported to this date.

CIO, Leon Guanajuato, Mexico. 15 April 2017.

**OCIS codes:** (120.0120) Instrumentation, measurement, and metrology; (100.2650) Fringe analysis; (120.6650) Surface measurements, figure.

---

## References and links

1. K. J. Gasvik, *Optical Metrology*, 3th ed., (John Wiley & Sons, 2002).
2. M. Servin, J. A. Quiroga, and M. Padilla, *Interferogram Analysis for Optical Metrology, Theoretical principles and applications* (Wiley-VCH, 2014).
3. J. C. Wyant, "Testing aspherics using two-wavelength holography," *Appl. Opt.* **10**, 2113–2118 (1971).
4. C. Polhemus, "Two-wavelength interferometry," *Appl. Opt.* **12**, 2071–2074 (1973).
5. Y. Y. Cheng and J.C. Wyant, "Multiple-wavelength phase-shifting interferometry," *Appl. Opt.* **24**, 804–807 (1985).
6. Y. Y. Cheng and J.C. Wyant, "Two-wavelength phase shifting interferometry," *Appl. Opt.* **23**, 4539–4543 (1984).
7. R. Onodera and Y. Ishii, "Two-wavelength interferometry that uses a Fourier-transform method," *Appl. Opt.* **37**, 7988–7994 (1998).
8. J. Kühn, T. Colomb, F. Montfort, F. Charrière, Y. Emery, E. Cuhe, P. Marquet, and C. Depeursinge, "Real-time dual-wavelength digital holographic microscopy with a single hologram acquisition," *Opt. Express* **15**, 7231–7242 (2007).
9. K. Falaggis, D. P. Towers, and C. E. Towers, "Multiwavelength interferometry: extended range metrology," *Opt. Lett.* **34**, 950-952 (2009).
10. T. Kakue, Y. Moritani, K. Ito, Y. Shimosato, Y. Awatsuji, K. Nishio, S. Ura, T. Kubota, and O. Matoba, "Image quality improvement of parallel four-step phase-shifting digital holography by using the algorithm of parallel two-step phase-shifting digital holography," *Opt. Express* **18**, 9555–9560 (2010).
11. C. Wagner, W. Osten, and S. Seebacher, "Direct shape measurement by digital wavefront reconstruction and multiwavelength contouring," *Opt. Eng.* **39**, 79–85 (2000).
12. D. Abdelsalam and D. Kim, "Two-wavelength in-line phase-shifting interferometry based on polarizing separation for accurate surface profiling," *Appl. Opt.* **50**, 6153–6161 (2011)

13. J. Li, L. G. Hassebrook, and C. Guan, "Optimized two-frequency phase-measuring-profilometry light-sensor temporal-noise sensitivity," *J. Opt. Soc. Am. A* 20, 108-115 (2003).
14. E. H. Kim, J. Hahn, H. Kim, B. Lee, "Profilometry without phase unwrapping using multi-frequency and four-step phase-shift sinusoidal fringe projection," *Opt. Express* 17, 7818-7830 (2009).
15. K. Liu, Y. Wang, D. L. Lau, Q. Hao, L. G. Hassebrook, "Dual-frequency pattern scheme for high-speed 3-D shape measurement," *Opt. Express* 18, 5229-5244 (2010).
16. Y. Xu, S. Jia, X. Luo, J. Yang, Y. Zhang, "Multi-frequency projected fringe profilometry for measuring objects with large depth discontinuities," *Opt. Comm.* 288, 27-30 (2013).
17. T. Liu, C. Zhou, Y. Liu, S. Si, Z. Lei, "Deflectometry for phase retrieval using a composite fringe," *Opt. Applicata* 94, 451-461 (2014).
18. Y. Xu, S. Jia, Q. Bao, H. Chen, J. Yang, "Recovery of absolute height from wrapped phase maps for fringe projection profilometry," *Opt. Express* 22, 16819 (2014).
19. W. Zhang, X. Lu, L. Fei, H. Zhao, H. Wang, and L. Zhong, "Simultaneous phase-shifting dual-wavelength interferometry based on two-step demodulation algorithm," *Opt. Lett.* 39, 5375-5378 (2014).
20. J. Long, J. Xi, M. Zhu, W. Cheng, R. Cheng, Z. Li, Y. Shi, "Absolute phase map recovery of two fringe patterns with flexible selection of fringe wavelengths," *Appl. Opt.* 53, 1794-1801 (2014).
21. J. M. Huntley and H. Saldner, "Temporal phase unwrapping algorithm for automated interferogram analysis," *Appl. Opt.* 32, (1993).
22. H. O. Saldner and J. M. Huntley, "Temporal phase unwrapping: application to surface profiling of discontinuous objects," *Appl. Opt.* 36, 2770-2775 (1997).
23. G. Pedrini, I. Alexeenko, W. Osten, H. J. Tiziani, "Temporal phase unwrapping of digital hologram sequences," *Appl. Opt.* 42, 5846-5854 (2003).
24. M. Servin, J. M. Padilla, A. Gonzalez, and G. Garnica, "Temporal phase-unwrapping of static surfaces with 2-sensitivity fringe-patterns," *Opt. Express* 23(12), 15806-15815 (2015).
25. M. Servin, M. Padilla, G. Garnica, and A. Gonzalez, "Profilometry of three-dimensional discontinuous solids by combining two-steps temporal phase unwrapping, co-phased profilometry and phase-shifting interferometry," *Opt. Laser Eng.* 87, 75-82 (2016).
26. A. Papoulis, *Probability, Random Variables and Stochastic Processes*, 4th ed. (McGraw Hill, 2000).

---

## 1. Introduction

Fringe-projection profilometry is well known and has widely been used for many years to obtain the form of solids in optical metrology [1,2]. Here we present an extended depth-range fringe-projection profilometry technique which uses two close-sensitivity fringe-patterns. It uses the well known concept of equivalent lambda interferometry [3]. Early double-wavelength interferometric experiments used two close laser wavelengths  $\{\lambda_1, \lambda_2\}$  ( $\lambda_1 \approx \lambda_2$ ) for optical testing of aspheric wavefronts [3-6]. Wyant used [3] two close laser-wavelengths  $\{\lambda_1, \lambda_2\}$  to test an optical surface with an equivalent wavelength of,

$$\lambda_{eq} = \frac{\lambda_1 \lambda_2}{|\lambda_1 - \lambda_2|} \quad (1)$$

Given that  $\lambda_1 \approx \lambda_2$ , the equivalent wavelength  $\lambda_{eq}$  is much larger than either  $\lambda_1$  or  $\lambda_2$ , *i.e.*  $\lambda_{eq} \gg \{\lambda_1, \lambda_2\}$ . The wavelength  $\lambda_{eq}$  is obtained by the following phase-difference,

$$\frac{2\pi}{\lambda_1} W(x, y) - \frac{2\pi}{\lambda_2} W(x, y) = \frac{2\pi}{\lambda_{eq}} W(x, y) \quad (2)$$

Being  $W(x, y)$  the optical wavefront. Double-wavelength interferometry was improved by Polhemus [4] and later on by Cheng [5,6] using digital phase-shifting phase-demodulation. Afterwards Onodera et al. used Fourier phase-demodulation methods for profiling structures with equivalent lambda depth size [7]. Unfortunately, the demodulated phase was over-smoothed due to the over filtering of too close Fourier diffraction orders [7]. This in turn was followed by a large number of double-wavelength Fourier and phase-shifting phase-demodulation methods in such diverse applications as double-wave holographic microscopy [8], extended range optical metrology [9], two-step digital holography [10], multiwavelength

extended-range contouring [11], and two-wavelength surface profiling [12]. Even though these methods [3-12] were applied to a variety of different experimental situations, all of them share the same mathematical background which may succinctly stated as follows: given two laser-interferometric phases  $\varphi_1(x, y) = (2\pi / \lambda_1)W(x, y)$  and  $\varphi_2(x, y) = (2\pi / \lambda_2)W(x, y)$ , calculate their phase difference  $\varphi_D(x, y) = \varphi_2(x, y) - \varphi_1(x, y)$  such that  $\varphi_D(x, y)$  is not-wrapped  $\varphi_D(x, y) \in (0, 2\pi)$ . In this way researches may claim having high depth-range measuring capabilities and having an additional bonus that they do not required any phase-unwrapping.

Laser dual-wavelength interferometric theory has been applied to three-dimensional (3D) fringe-projection profilometry and contouring [13-20]. These methods have been called among other, two-frequency profilometry [13], profilometry without phase unwrapping [14], dual-frequency shape measurement [15], large-depth discontinuous objects profilometry [16], deflectometry of composite fringe phase retrieval [17], absolute-height fringe-projection profilometry [18], dual-wavelength two-steps phase-shifting demodulation [19], two fringe patterns absolute-phase recovery [20]. All these techniques end up obtaining an unwrapped, extended depth-range, phase-difference  $\varphi_D(x, y) = \varphi_2(x, y) - \varphi_1(x, y)$  of two close-sensitive phase measurements. If the experiment is properly made, this phase-difference is not-wrapped *i.e.*  $\varphi_D(x, y) \in (0, 2\pi)$ . As mentioned, these authors refer to their digital interferometric techniques as extended-range, absolute-phase measurement, interferometry without phase-unwrapping or direct shape measurement [13-20].

Previous close phase-sensitivity extended-range profilometers rely only on the phase difference  $\varphi_D(x, y) \in (0, 2\pi)$ , and do not use the phase-sum  $\varphi_S(x, y)$ ; even though this is readily available from their fringe-data. Why should anyone bother to use  $\varphi_S(x, y)$ ? The non-wrapped phase-difference  $\varphi_D(x, y)$  contains the searched extended-range phase-profile and it is already unwrapped. Why anyone should look for the phase-sum?. Here we conjecture two reasons why the phase-sum have never been used,

- a) When researchers began to apply close-sensitivity double-wave digital interferometric ideas to digital profilometry [14-20], by tradition (we believe) they continued to use just the phase-difference  $\varphi_D(x, y)$ . However they could easily find the higher quality phase-sum  $\varphi_S(x, y)$  from the same fringe data, but they did not see any reason or necessity of using the highly wrapped phase-sum [5-20].
- b) Computing the phase-sum of two close-sensitivity phases did not have much appeal because spatial unwrapping of  $\varphi_S(x, y)$  for discontinuous or separate objects is precluded. The only choice was Huntley's temporal phase unwrapping [21, 23]. But Huntley's temporal unwrapping needs a series of increasing sensitivity phase maps at the Nyquist temporal rate. This would require to have many intermediate temporal phases [21,23]; not just the two extremes  $\varphi_D(x, y)$  and  $\varphi_S(x, y)$ .

So there was no motivation for dealing with the highly wrapped phase-sum; nobody knew how to temporally unwrap  $\varphi_S(x, y)$  from  $\varphi_D(x, y)$ . Also nobody knew that  $\varphi_S(x, y)$  has much higher signal-to-noise ratio than  $\varphi_D(x, y)$  [3-20].

Here we first demodulate two close-sensitivity solid's phases  $\varphi_1(x, y)$  and  $\varphi_2(x, y)$ . From them we calculate  $\varphi_D(x, y) = \varphi_2(x, y) - \varphi_1(x, y)$  and  $\varphi_S(x, y) = \varphi_1(x, y) + \varphi_2(x, y)$ . We then temporarily unwrap  $\varphi_S(x, y)$  directly from  $\varphi_D(x, y)$  using our 2-step extended-range temporal phase-unwrapping [24, 25]. Extended temporal phase-unwrapping of static objects, allows us to circumvent the Nyquist temporal sampling limit, overcoming the need of many intermediate wrapped-phases [24,25]. Finally we are using the complex-valued analytic

formalism for the phase-shifting algorithms [2, 26] and use some elementary facts of random process applied to linear systems [27].

## 2. High depth-range profilometry using phase-difference and phase-sum

Digital fringe-projection profilometry is a well known technique that has been used for many years [1]. An experimental set up for three-dimensional (3D) profilometry of solids is shown in Fig. 1.

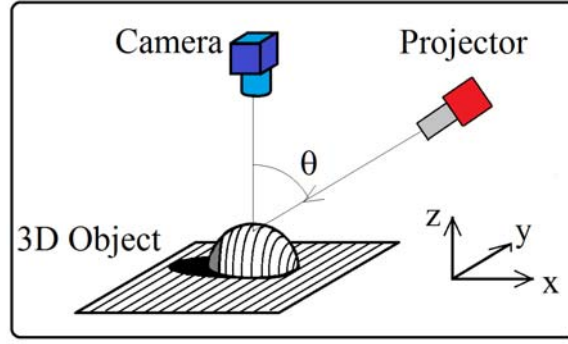


Fig. 1. Schematic of a fringe-projection profilometer. The digitizing solid is a sphere segment and  $\theta$  is the sensitivity angle of this profilometer.

The mathematical model for the fringes  $I_1(x, y)$  and  $I_2(x, y)$  taken by the CCD camera are,

$$\begin{aligned} I_1(x, y, n) &= a(x, y) + b(x, y) \cos \left[ u_1 \tan(\theta) h(x, y) + u_1 x + \frac{2\pi}{4} n \right]; \\ I_2(x, y, n) &= a(x, y) + b(x, y) \cos \left[ u_2 \tan(\theta) h(x, y) + u_2 x + \frac{2\pi}{4} n \right]; \quad n = \{0.1.2.3\}. \end{aligned} \quad (3)$$

Where  $a(x, y)$  is the background illumination;  $b(x, y)$  the fringe contrast;  $h(x, y)$  the solid height and  $\theta$  the profilometer's sensitivity angle. Finally the spatial-carrier frequencies are  $u_1 = 2\pi / p_1$  and  $u_2 = 2\pi / p_2$  in radians/pixel. The parameters  $p_1$  and  $p_2$  are the periods of the projected-fringes in pixels. They have very close real-values  $p_1 \approx p_2$ .

### 2.1 Phase-difference and phase-sum estimations for high depth-range profilometry

Using the least-squares 4-step phase-shifting algorithm we demodulate the fringes in Eq. (3) [2] obtaining the complex-valued analytic signals,

$$\begin{aligned} A_1(x, y) e^{i\varphi_1(x, y)} &= e^{-iu_1 x} \left[ \sum_{n=0}^3 I_1(x, y, n) e^{i\left(\frac{2\pi}{4}\right)n} \right], \\ A_2(x, y) e^{i\varphi_2(x, y)} &= e^{-iu_2 x} \left[ \sum_{n=0}^3 I_2(x, y, n) e^{i\left(\frac{2\pi}{4}\right)n} \right]. \end{aligned} \quad (4)$$

Where  $\varphi_1(x, y) = u_1 \tan(\theta) h(x, y)$  and  $\varphi_2(x, y) = u_2 \tan(\theta) h(x, y)$ , and the reference planes  $\exp(iu_1 x)$  and  $\exp(iu_2 x)$  were removed. It is well known that 3 phase-shifted fringes (phase-shift  $2\pi/3$  rad.) is the minimum number of fringe-patterns [2]. However increasing to 4-steps (phase-shift  $2\pi/4$  rad.) phase-shifted fringes one decreases substantially the harmonic content in the demodulated phase as Fig. 2 shows [2].

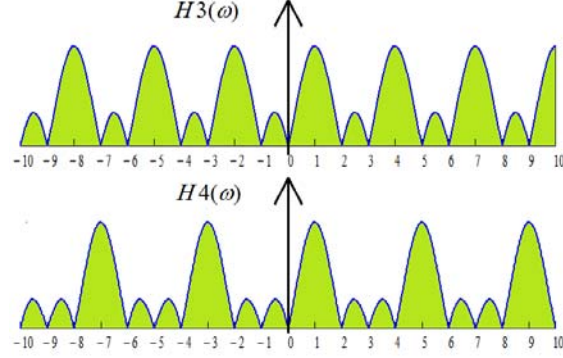


Fig. 2. Normalized frequency-transfer-functions (FTFs) for 3 and 4-step PSAs.  $H3(\omega)$  passes high-amplitude harmonics  $\{-2,4\}$ , while  $H4(\omega)$  passes more distant harmonics  $\{-3,5\}$ . This harmonics rejection gain of  $H4(\omega)$  with respect to  $H3(\omega)$  makes  $H4(\omega)$  a much better option.

Then the following products are computed,

$$\begin{aligned} A_1 e^{i\varphi_1(x,y)} [A_2 e^{i\varphi_2(x,y)}]^* &= A_1 A_2^* e^{i[\varphi_1(x,y) - \varphi_2(x,y)]}, \\ A_1 e^{i\varphi_1(x,y)} [A_2 e^{i\varphi_2(x,y)}] &= A_1 A_2 e^{i[\varphi_1(x,y) + \varphi_2(x,y)]}. \end{aligned} \quad (5)$$

The two fringe periods  $p_1$  and  $p_2$  are chosen close enough so the phase difference,

$$\varphi_D(x, y) = \text{angle} [A_1 A_2^* e^{i[\varphi_1(x,y) - \varphi_2(x,y)]}], \quad (6)$$

is not-wrapped *i.e.*  $\varphi_D(x, y) \in (0, 2\pi)$ . However the phase sum  $\varphi_S^W(x, y)$ ,

$$\varphi_S^W(x, y) = \text{angle} [A_1 A_2 e^{i[\varphi_1(x,y) + \varphi_2(x,y)]}], \quad (7)$$

is highly wrapped because it has the sensitivity of  $\varphi_1(x, y) + \varphi_2(x, y)$ . The phase-difference and the phase-sum have equivalent projected fringe periods of,

$$\begin{aligned} \frac{2\pi}{p_1} \tan(\theta) h(x, y) - \frac{2\pi}{p_2} \tan(\theta) h(x, y) &= \frac{2\pi}{p_D} \tan(\theta) h(x, y) \\ \frac{2\pi}{p_1} \tan(\theta) h(x, y) + \frac{2\pi}{p_2} \tan(\theta) h(x, y) &= \frac{2\pi}{p_S} \tan(\theta) h(x, y), \end{aligned} \quad (8)$$

From this equation one may derive the equivalent fringe periods  $p_D$  and  $p_S$  as,

$$\begin{aligned} p_D &= \frac{p_1 p_2}{|p_1 - p_2|}; & \text{for } \varphi_1(x, y) - \varphi_2(x, y), \\ p_S &= \frac{p_1 p_2}{p_1 + p_2}; & \text{for } \varphi_1(x, y) + \varphi_2(x, y). \end{aligned} \quad (9)$$

Note that formulas for  $p_D$  and  $\lambda_{eq}$  are formally identical. As a consequence if  $p_1 \approx p_2$ , then  $p_D$  is much larger than  $p_1$  or  $p_2$ ; *i.e.*  $p_D \gg \{p_1, p_2\}$ . In contrast  $p_S$  is much shorter than either  $p_1$  or  $p_2$ ; *i.e.*  $p_S \ll \{p_1, p_2\}$ . This makes the phase difference  $\varphi_D(x, y)$  to have low-sensitivity while  $\varphi_S(x, y)$  to have high sensitivity. Then the sensitivity gain  $G$  between the phase-difference and phase-sum is,

$$G = \frac{\|\varphi_s(x, y)\|}{\|\varphi_D(x, y)\|} = \frac{\|(u_2 + u_1) \tan(\theta) h(x, y)\|}{\|(u_2 - u_1) \tan(\theta) h(x, y)\|} = \frac{u_1 + u_2}{|u_1 - u_2|}, \quad (10)$$

Where  $\|\cdot\|$  stand for the maximum norm. Substituting  $u_1 = 2\pi / p_1$  and  $u_2 = 2\pi / p_2$  we get,

$$G = \frac{u_2 + u_1}{|u_2 - u_1|} = \frac{p_1 + p_2}{|p_1 - p_2|} = \frac{p_D}{p_s}, \quad (11)$$

Meaning that the phase-sensitivity gain between  $\varphi_D(x, y)$  and unwrapped  $\varphi_s(x, y)$  is,

$$\varphi_s(x, y) = \frac{u_2 + u_1}{|u_2 - u_1|} \varphi_D(x, y). \quad (12)$$

In other words,  $\varphi_s(x, y)$  is  $G$  times more sensitive than  $\varphi_D(x, y)$ .

### 2.2 Extended-range temporal 2-steps phase unwrapping

In this paper, the non-wrapped  $\varphi_D(x, y) \in (0, 2\pi)$  is used as first estimation to temporarily unwrap  $\varphi_s^W(x, y) = W[\varphi_s(x, y)]$  in just two steps; being  $W[x] = \text{angle}[\exp(ix)]$ . The extended-range 2-steps temporal phase-unwrapping formula is [24,25],

$$\varphi_s(x, y) = \frac{p_D}{p_s} \varphi_D(x, y) + W \left[ \varphi_s^W(x, y) - \frac{p_D}{p_s} \varphi_D(x, y) \right]. \quad (13)$$

The two conditions that need to be fulfilled for the above equation are,

$$\varphi_D(x, y) \in (0, 2\pi), \quad \text{and} \quad [\varphi_s(x, y) - G \varphi_D(x, y)] \in (0, 2\pi). \quad (14)$$

If these conditions are not fulfilled, the 2-steps temporal phase-unwrapping do not work [24].

An additional advantage of extended-range temporal unwrapping in Eq. (13) is its immunity to the phase errors (harmonics and noise) of  $\varphi_D(x, y)$  [24]. This means that having the erroneous phases,

$$\begin{aligned} \varphi_D(x, y) &= \varphi_1(x, y) - \varphi_2(x, y) + e_D(x, y), \\ \varphi_s^W(x, y) &= W[\varphi_1(x, y) + \varphi_2(x, y) + e_s(x, y)]. \end{aligned} \quad (15)$$

Being  $e_D(x, y)$  and  $e_s(x, y)$  the degrading noise and harmonics. The unwrapped phase  $\varphi_s(x, y)$  in Eq. (13) contains only its own degrading signals,

$$\varphi_s(x, y) = \varphi_1(x, y) + \varphi_2(x, y) + e_s(x, y). \quad (16)$$

The phase error  $e_D(x, y)$  in  $\varphi_D(x, y)$  do not propagate towards the unwrapped  $\varphi_s(x, y)$ . This was mathematically proven in [24].

### 3. Signal-to-noise ratio between the phase-sum and phase-difference

In practice the phase-shifting demodulated phases  $\varphi_1(x, y)$  and  $\varphi_2(x, y)$  are always corrupted by white Gaussian noise [26]. Therefore the demodulated phases are the sum of the solid's phase plus a measuring phase-noise as,

$$\begin{aligned} \varphi_1(x, y) &= u_1 \tan(\theta) h(x, y) + n_1(x, y); \\ \varphi_2(x, y) &= u_2 \tan(\theta) h(x, y) + n_2(x, y). \end{aligned} \quad (17)$$

Where  $n_1(x, y)$  and  $n_2(x, y)$  ( $n_2(x, y) \neq n_1(x, y)$ ) are two samples of the same wide-sense stationary random process [26]. The noise fields  $n_1(x, y)$  and  $n_2(x, y)$  have the same ensemble average  $\mu$ , standard deviation  $\sigma^2$  and autocorrelation function  $R(\xi, \eta)$ ,

$$\begin{aligned}\mu &= E\{n_1(x, y)\} = E\{n_2(x, y)\}; \\ \sigma^2 &= E\{n_1^2(x, y)\} = E\{n_2^2(x, y)\} = R(0, 0); \\ R(\xi, \eta) &= E\{n_1(x, y)n_1(x + \xi, y + \eta)\} = E\{n_2(x, y)n_2(x + \xi, y + \eta)\}.\end{aligned}\quad (18)$$

Where  $E\{\cdot\}$  is the ensemble average of its argument [32]. Also it is assumed that the noise energy is low *i.e.*  $\sigma^2 \ll 2\pi$ . Using Eq. (17), the phase-difference and phase-sum are,

$$\begin{aligned}\varphi_D(x, y) &= (u_2 - u_1) \tan(\theta) h(x, y) + n_2(x, y) - n_1(x, y); \\ \varphi_S(x, y) &= (u_2 + u_1) \tan(\theta) h(x, y) + n_2(x, y) + n_1(x, y).\end{aligned}\quad (19)$$

On the other hand we know that  $\iint |f(x, y)|^2 d\Omega$  and  $(1/A_\Omega) \iint |f(x, y)|^2 d\Omega$  are the energy and power of a signal  $f(x, y)$ ; being  $A_\Omega$  the area of well-defined fringe-data  $\Omega$ . Then the signal-to-noise power-ratio for  $\varphi_D(x, y)$  and  $\varphi_S(x, y)$  are,

$$\begin{aligned}\left(\frac{S}{N}\right)_{\varphi_D(x, y)} &= \frac{\iint_{(x, y) \in \Omega} |\varphi_D(x, y)|^2 d\Omega}{\iint_{(x, y) \in \Omega} |n_D(x, y)|^2 d\Omega} = \frac{(u_2 - u_1)^2 \tan^2(\theta) \iint_{(x, y) \in \Omega} |h(x, y)|^2 d\Omega}{\iint_{(x, y) \in \Omega} |n_2(x, y) - n_1(x, y)|^2 d\Omega}; \\ \left(\frac{S}{N}\right)_{\varphi_S(x, y)} &= \frac{\iint_{(x, y) \in \Omega} |\varphi_S(x, y)|^2 d\Omega}{\iint_{(x, y) \in \Omega} |n_S(x, y)|^2 d\Omega} = \frac{(u_2 + u_1)^2 \tan^2(\theta) \iint_{(x, y) \in \Omega} |h(x, y)|^2 d\Omega}{\iint_{(x, y) \in \Omega} |n_2(x, y) + n_1(x, y)|^2 d\Omega}.\end{aligned}\quad (20)$$

Given that both noise samples are generated by the same Gaussian zero-mean stationary random process, *in the average*, the energy of  $n_2(x, y) - n_1(x, y)$  and  $n_2(x, y) + n_1(x, y)$  are equal [26],

$$\iint_{(x, y) \in \Omega} |n_2(x, y) - n_1(x, y)|^2 d\Omega = \iint_{(x, y) \in \Omega} |n_2(x, y) + n_1(x, y)|^2 d\Omega.\quad (21)$$

Therefore, the signal-to-noise power-ratio gain between  $\varphi_S(x, y)$  and  $\varphi_D(x, y)$  is,

$$\frac{(S/N)_{\varphi_S(x, y)}}{(S/N)_{\varphi_D(x, y)}} = \frac{(u_2 + u_1)^2}{(u_2 - u_1)^2} = \left(\frac{p_D}{p_S}\right)^2 = G^2.\quad (22)$$

In conclusion, the phase-sum  $\varphi_S(x, y)$  has  $(p_D / p_S)^2$  higher signal-to-noise power-ratio than  $\varphi_D(x, y)$  [24, 25]. This is a huge motivation for using  $\varphi_S(x, y)$ .

#### 4. Experiments in extended depth-range profilometry

So far we have mathematically demonstrated the higher phase-sensitivity and higher signal-to-noise ratio of our extended depth-range two-sensitivity profilometer with respect to previous extended-range profilometers that used only the phase-difference [13-20]. In this section we show two experimental examples to make this extended depth-range profilometry technique better understandable.

#### 4.1 Extended depth-range profilometry of a spherical metallic cap

A spherical metallic cap used as calibrating solid is shown in Fig. 3. This is a regular photograph, not a three-dimensional (3D) digital rendering.

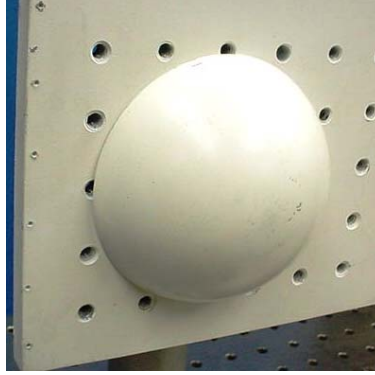


Fig. 3. Photograph of the calibrating spherical metallic cap. Although this solid is smooth, it was digitized to demonstrate beyond any doubt, the high sensitivity gain of our 2-sensitivity profilometer compared to previous extended-range profilometry techniques.

In Fig. 4 we show the two close spatial-frequencies (close phase-sensitivities) linear-fringes projected on this spherical object.

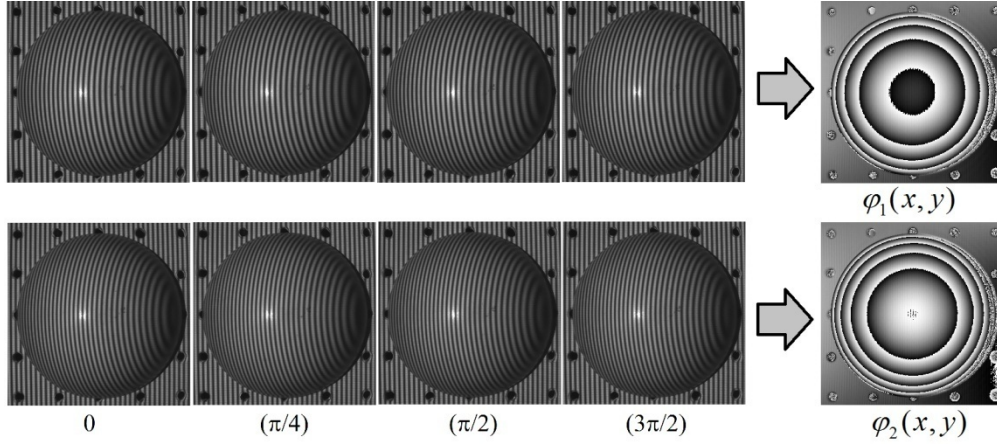


Fig. 4. A metallic spherical segment illuminated by two linear fringes and their phase demodulation. The phase-shifting among the fringe-patterns are  $\{0, \pi/4, \pi/2, 3\pi/2\}$ . The upper row has lower phase-sensitivity fringes than the lower row. The right column shows the demodulated wrapped phases.

In the upper row of Fig. 4, we have projected linear-fringes with spatial-frequency of  $u_1 = 2\pi/7$  radians/pixel. In the lower row we have projected linear-fringes with a spatial frequency  $u_2 = 2\pi/6$  radians/pixel. The phase-sensitivity of the fringes with spatial-frequency  $u_2$  is higher than the fringes at frequency  $u_1$ .

In Fig. 5 we show the phase-subtraction operation (upper row) and the phase-addition operation (lower row) of the two demodulated phases in Fig. 4. The sensitivity gain  $G$  is then given by,

$$G = \frac{u_1 + u_2}{|u_1 - u_2|} = \frac{(2\pi/6 + 2\pi/7) \text{ Radians / Pixel}}{|2\pi/6 - 2\pi/7| \text{ Radians / Pixel}} = 13, \quad (23)$$

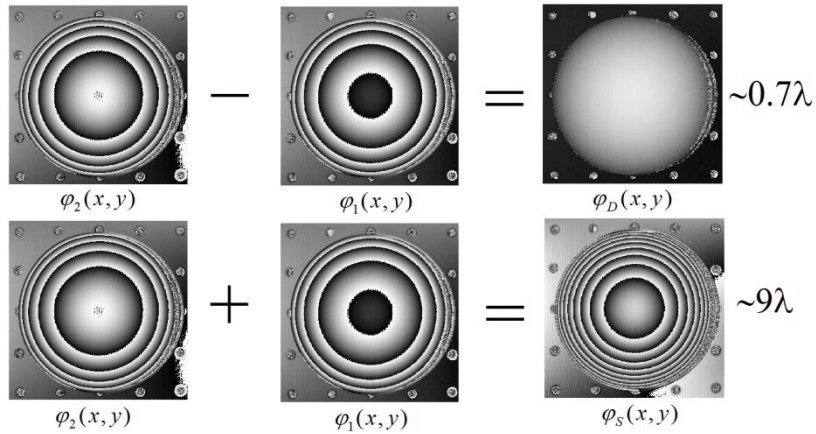


Fig. 5. The upper row graphically shows the phase-difference while the lower row shows their phase-sum. The phase difference has about 0.7 lambda sensitivity so it is not-wrapped. The phase-sum is however wrapped about 9-times.

That is, we have 13-times more sensitivity in the phase-sum  $\varphi_S(x, y)$  compared to the non-wrapped phase-difference  $\varphi_D(x, y)$ .

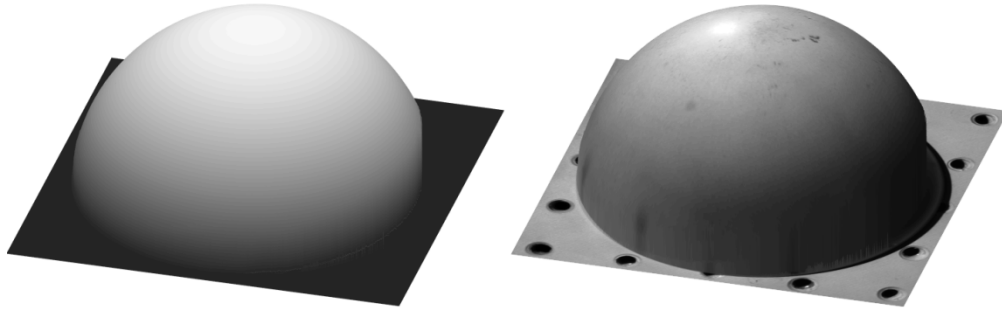


Fig. 6. Three-dimensional (3D) digital rendering of the recovered unwrapped phase-sum of the spheric solid. The left-side rendering is the gray-coded unwrapped phase-sum. For the right-side 3D digital rendering we use the spherical-cap photograph as texture.

Figure 6 shows the 2-steps unwrapped phase-sum  $\varphi_S(x, y)$  taking as first estimation the non-wrapped phase difference  $\varphi_D(x, y)$ . In Fig. 7 we show a central phase-cut of  $\varphi_D(x, y)$  and  $\varphi_S(x, y)$  to gauge the different amounts of degrading phase noise.

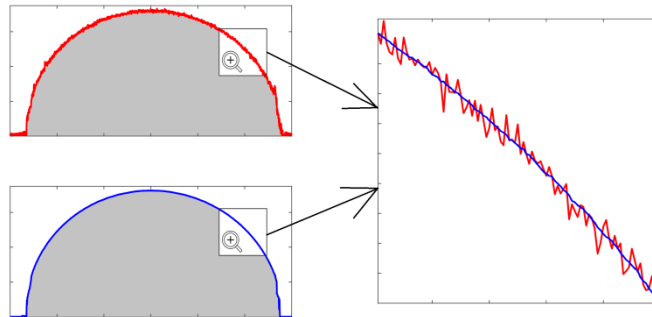


Fig. 7. A cut of the 3D rendering of the spherical metallic cap. The red trace is the phase-difference and the blue trace is the unwrapped phase-sum. We can see that the blue trace has significant lower phase-noise.

In the zoomed-in detail one may see the difference in noise amplitude corresponding to the noisier phase-difference in red, and the phase-sum in blue.

#### 4.2 Extended depth-range profilometry of a fluorescent spiral light bulb

Figure 8 shows our next object to be digitized; a spiral fluorescent lamp. This is a regular photography not a 3D digital rendering.



Fig. 8. Regular Photograph (not 3D rendering) of a spiral fluorescent lamp under analysis.

Figure 9 shows the phase-shifted linear-fringes of lower and higher spatial frequencies. In the upper row we have projected a spatial frequency of  $u_1 = 2\pi/9$  radians/pixel. In the lower row we have projected a spatial frequency of  $u_2 = 2\pi/8$  radians/pixel.

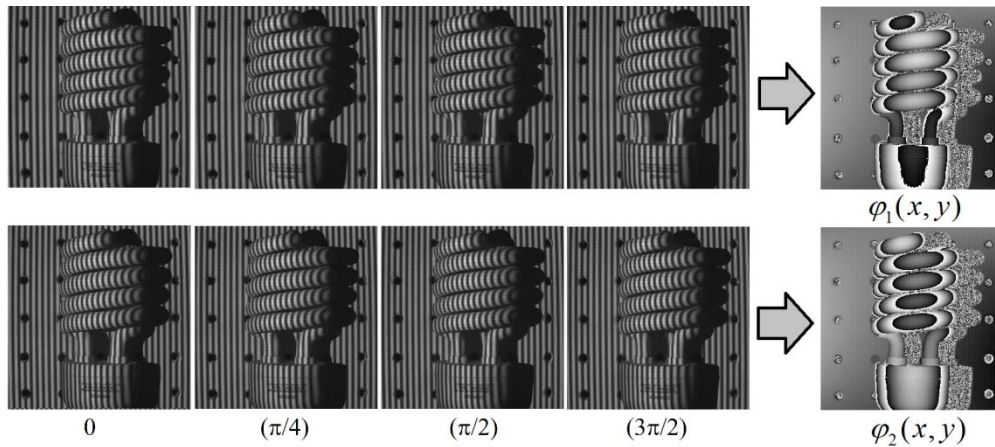


Fig. 9. The spiral lamp illuminated by two close spatial-frequency linear fringes. The lower spatial frequency fringes are shown in the first row; the higher spatial frequency fringes are shown in the lower row. Their wrapped 4-step phase-shifting demodulated phases are shown at the right-side column.

Figure 10 shows the phase-difference  $\varphi_D(x, y)$  and phase-sum  $\varphi_S(x, y)$  operations of the two sensitivities demodulated phase-maps in Fig. 9.

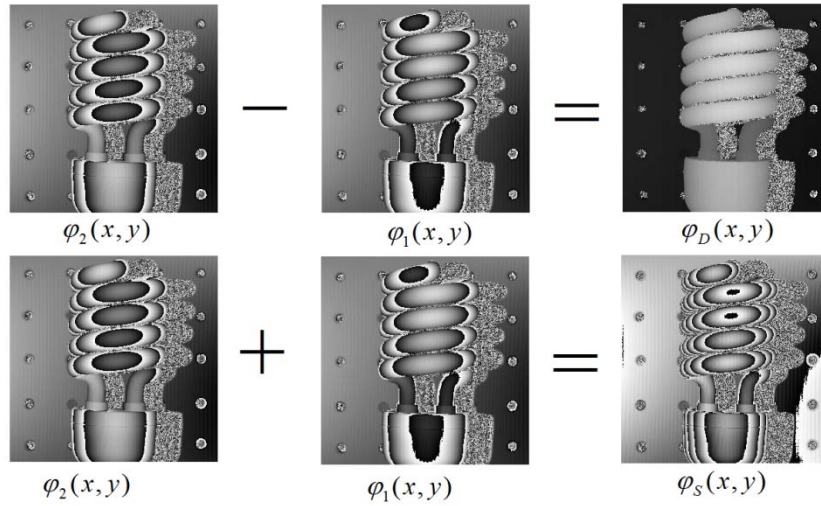


Fig. 10. The upper row shows the phase-difference operation while the lower row shows the phase-sum operation. The phase difference is not-wrapped. The phase-sum has however much higher phase sensitivity, so it is highly wrapped.

The sensitivity gain  $G$  in the spiral-lamp case is given by,

$$G = \frac{u_1 + u_2}{|u_1 - u_2|} = \frac{(2\pi / 8 + 2\pi / 9) \text{ Radians / Pixel}}{|2\pi / 8 - 2\pi / 9| \text{ Radians / Pixel}} = 17, \quad (24)$$

That is, we have 17-times more sensitivity in the phase-sum  $\varphi_S(x, y)$  compared to the phase-difference  $\varphi_D(x, y)$ .

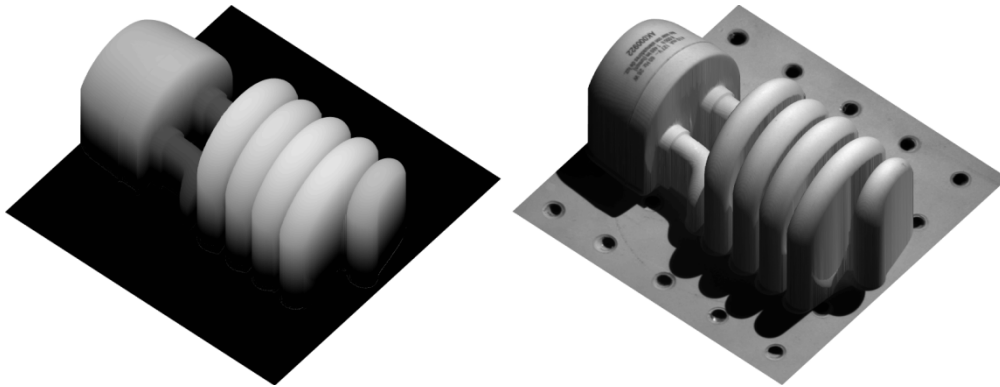


Fig. 11. Three-dimensional (3D) digital rendering of the recovered unwrapped phase-sum. The left-side rendering is a gray-coded phase. For the right-side rendering we used a photograph of the lamp as rendering texture over the unwrapped phase-sum.

Figure 11 shows the two-step extended-range temporal unwrapped-phase of the highest sensitivity phase-sum.

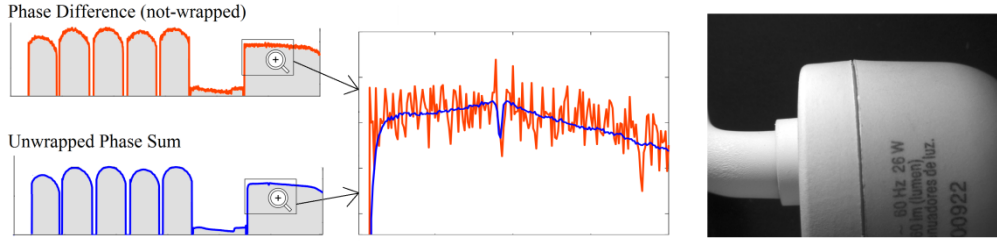


Fig. 12. We show a cut to compare the signal-to-noise gain between the phase-difference (in red), and the phase-sum (in blue). We have zoomed-in into the rectangle shown to clearly see the depression (in blue) at the joining of the two plastic pieces shown at the right photograph-detail.

Figure 12 shows two phase-cuts of the digitized 3D rendering of the spiral fluorescent lamp. In the far right photograph a regular zoom-in photograph is shown to see the joint between these two plastic pieces. This plastic joint depression is hardly seen in the red-graph because it is immersed in measuring noise.

## 5. Summary

We have presented a two-sensitivity extended depth-range (or absolute phase) fringe-projection profilometry technique. This two-sensitivity profilometry method uses two sets of phase-shifted linear-fringe projections to obtain the phases  $\varphi_1(x, y)$  and  $\varphi_2(x, y)$ . From these phases, we compute their phase-difference  $\varphi_D(x, y) = \varphi_2(x, y) - \varphi_1(x, y)$  and their phase-sum  $\varphi_S(x, y) = \varphi_1(x, y) + \varphi_2(x, y)$ . The phase-sensitivity between  $\varphi_1(x, y)$  and  $\varphi_2(x, y)$  is made close enough so their difference is non-wrapped *i.e.*  $\varphi_D(x, y) \in (0, 2\pi)$ . In contrast the high-sensitivity phase-sum  $\varphi_S(x, y)$  is highly wrapped. Finally we used an extended-range 2-steps temporal phase-unwrapper to unwrap  $\varphi_S(x, y)$  taking  $\varphi_D(x, y)$  as first estimation. As far as we know this is the highest sensitivity, highest signal-to-noise ratio 2-sensitivity profilometry technique to this day.

At the risk of being repetitive we want to clearly point-out the main contributions of this paper as follows,

- a) Previous dual-frequency close-sensitivity extended-range profilometers used just the phase-difference of two sets of fringe-patterns. Researchers had no motivation, interest and/or knowledge for using the phase-sum of their phase estimations to improve the signal-to-noise ratio of their profilometry measurements [3-20].
- b) The phase-difference of two close-sensitivity phase-modulated linear fringes has the advantage that no phase unwrapping is needed, *i.e.*  $\varphi_D(x, y) \in (0, 2\pi)$ . That is why we believe, previous workers in this field stopped this far [3-20].
- c) But as shown herein, ignoring the phase-sum and relying on the phase-difference only, one gets a lower phase-sensitivity and noisier profilometry measurements.
- d) In contrast the phase-sum  $\varphi_S(x, y)$  has much higher phase-sensitivity and signal-to-noise ratio but it is highly wrapped. Spatial phase-unwrapping of discontinuous or separated solids coded in  $\varphi_S(x, y)$  is therefore precluded. This is another reason (we believe) why previous researches had no interest in calculating the phase-sum.
- e) Different to previous efforts in this field, here we are productively combining the information provided by both: the non-wrapped low-sensitivity phase-difference  $\varphi_D(x, y)$  and previously neglected phase-sum  $\varphi_S(x, y)$  [3-20].

- f) To compute  $\varphi_s(x, y)$  no additional fringes to that previously needed to obtain  $\varphi_D(x, y)$  are necessary. Therefore with the theory given herein, legacy fringe-patterns may now be used to obtain higher quality profilometry measurements by just calculating and temporarily unwrapping the formerly ignored phase-sum; *i.e.* no need of new or additional fringe data is necessary.
- g) Finally we can easily unwrap the higher quality phase-sum  $\varphi_s(x, y)$  taking the phase-difference  $\varphi_D(x, y)$  as first estimation using our previously published 2-steps extended-range temporal phase unwrapper [24, 25].